Journal of Alloys and Compounds 919 (2022) 165835

Contents lists available at ScienceDirect

Journal of Alloys and Compounds

journal homepage: www.elsevier.com/locate/jalcom

Benzoate anion derived carbon-encapsulated NiS nanoparticles as a freestanding cathode for magnesium-based batteries

Guilei Zhu, Wenbin Wang, Xuebin Yu*

Department of Materials Science, Fudan University, Shanghai 200433, China

ARTICLE INFO

Article history:
Received 29 March 2022
Received in revised form 6 June 2022
Accepted 9 June 2022
Available online 13 June 2022

Keywords:
Self-supported cathode
Ultrafine nanoparticles
Carbon-wrapped nickel sulfide
Hybrid magnesium-based battery

ABSTRACT

Due to its wide diffusion channels and high electronic conductivity, conversion-type transition metal-based chalcogenide cathode materials are endowed greater potential to implement high capacity in Mg-based batteries. However, large coulombic interactions and sluggish kinetics at high charge density perplex its electrochemical performance, and application of which is also seriously hindered by large volume expansion. Herein, we design a facile approach to in-situ fabricate ultrafine and well-dispersive carbon encapsulated NiS nanoparticles anchored on carbon cloth (NiS@C NPs/CC) through one-step carbonization and sulfuration of benzoate anion-intercalated $Ni(OH)_2$ on CC. The as-prepared NiS@C NPs/CC is employed as the binder-free cathode material for hybrid Mg^{2+}/Li^+ batteries (MLIBs), whose energy storage capability is largely enhanced due to well-dispersive NiS nanoparticles. The MLIB assembled with NiS@C NPs/CC cathode implements a superior reversible capacity of 437 mAh g^{-1} at 100 mA g^{-1} and exhibits long lifespan. Its small diameter of 13.2 nm greatly shortens the ion transport pathway, and traits of carbon confinement and self-assembly synergistically boost electric conductivity at the same time, which contribute to the impressive electrochemical performance. This work not only realizes favorable synthesis of ultrafine and well-dispersive nanoparticles materials derived from the intercalation of organic-anion, but inaugurates a novel avenue for the rational design of carbon coated binder-free electrode for applications.

1. Introduction

Secondary batteries have become an indispensable energy source, providing a more environmentally friendly option to electronic systems than primaries, since they can be recharged rather than requiring new batteries, which are discarded when they are exhausted [1–4]. In recent years, however, highly safe and earth-abundant alternatives of lithium-ion batteries (LIBs) appeal to investigation, because a number of safety accidents of LIBs and ongoing lack of Li resource. Magnesium ion batteries (MIBs) are therefore emerging as a promising post-lithium energy storage system on account of high security (lower reducibility and much higher melting point) and high abundance (about 1000 times more than Li) of Mg metal [5–7]. In addition, Mg metal with two-charge carrier exhibits higher volumetric capacity and has the advantages of few dendrite and low reduction potential (−2.37 V vs. SHE), which all facilitate development of MIBs [8,9]. However, the exploration of suitable and effective cathode materials is still the foundation to meet the development of MIBs.

The diffusion kinetics of divalent Mg^{2+} is a crucial factor determining the electrochemical performance of MIBs. Unlike the sluggish Mg^{2+} kinetics in metal oxide lattices, Mg^{2+} migrates faster inside metal chalcogenides cathode materials [10–12]. For instance, the mobility of Mg^{2+} shows obvious difference in a system that employs MX_2 (where M = Mo, Ti, V; X = O, S, Se). Mg^{2+} transfers much more easily when the anion systematically alters from O_2^{2-} to Se^{2-}. Such phenomenon can be well explained by following three aspects. First, larger ion radii result in huger diffusion channel size; Second, the non-metallicity of the same group of non-metallic elements weakens as the number of periods increases, leading to an enhancement in electrical conductivity; Finally, the strength of the coulombic interaction between Mg^{2+} (hard acid) and softer anions (S^{2-} and Se^{2-}) is reduced, which generates a lower barrier for Mg^{2+} diffusion. Therefore, metal chalcogenides present potential to boost the kinetics of MIBs systems, thus attracting great attention as promising cathode materials for MIBs. Moreover, the hybrid Mg^{2+}/Li^+ batteries (MLIBs) constructed by incorporating Li^+ into the electrolyte can not only fully utilize the fast kinetic of Li^+ to insert into cathode, but also bypass the deposition of Li metal at the anode

* Corresponding author.
E-mail address: yuxuebin@fudan.edu.cn (X. Yu).

https://doi.org/10.1016/j.jallcom.2022.165835
0925-8388/

[13–16]. Such configuration has the ability to achieve higher reversible capacity and longer cycle life, and has been widely reported in various mental chalcogenides, such as V [17,18], Ti [19,20], Mo [21,22], Cu [13,23–26], Fe [27], Co [16,28,29], Ni [30] based materials. Among these typical conversion cathode materials, nickel-based sulfides stand out with merits of price moderate, environmental compatibility, diverse synthesis methods and high theoretical capacity, which lead to an extensive employment as electrode materials in various batteries [31–34]. U Unfortunately, the large volume expansion nature of nickel-based sulfides in conversion reactions gives rise to its low material utilization and poor capacity retention in MLIBs systems. In consequence, modifications that rationally design such materials and alleviate volume expansion are indispensable, as a result of which, the MLIBs system could implement an eminent electrochemical performance.

Recently, we report a series of size-controllable NiS nanoparticles embedded in carbon nanofibers via electrospinning technique and subsequent thermal treatment [30]. Excellent rate capability is accomplished in MLIBs through the optimization of particle size and carbon ratio, and corresponding conversion mechanism is also clearly demonstrated. To be more specific, the conversion of NiS in MLIBs involves two parts, including an irreversible conversion from NiS to Ni_3S_2 ($3(x + y)NiS + xMg^{2+} + y2Li^+ + 2(x + y)e^- \rightarrow (x + y)Ni_3S_2 + xMgS + yLi_2S$) and a reversible reaction from Ni_3S_2 to Ni ($0.5(x + y)Ni_3S_2 + xMg^{2+} + 2yLi^+ + 2(x + y)e^- \leftrightarrow 1.5(x + y)Ni + xMgS + yLi_2S$), where MgS product is generated during each transformation, indicating the involvement of Mg^{2+} in cathodic reaction. This study elucidates the feasibility of such materials in MLIBs and the improvement of kinetic properties via the tactic of carbon limitation. Meanwhile, the approaches of carbon encapsulation and the sources of carbon are characterized by diversity, including ex situ and in situ encapsulation [35–39]. As for ex situ fabrication, carbon products (such as carbon nanotubes, graphite, graphene, carbon fibers, carbon spheres, etc.) are generally fully mixed with materials. The most common method is ball milling, where plasma milling is a newer strategy that also effectively strips materials [40,41]. In terms of in situ synthetic method, carbon sources generally exist in precursors in the form of organic matter. Frequently, when using metal organic frame as a precursor for heat treatment, corresponding organic ligand is applied as a carbon source to realize high-conductivity carbon coated on the surface of active material. For a precursor with a layered structure, some organic anions of moderate size acted as carbon source can be inserted into the interlayer to accomplish carbon limitation after heat treatment, in which the diversity of organic anions makes this method plenty of unknown possibilities.

Nickel hydroxide is well known to be a layered structure with a layer spacing of 0.48 nm, into which benzoate (0.7 nm in length) also can be easily inserted [42]. Such size evaluations promise the feasibility to fabricate carbon-coated nanoparticles after thermal treatment. The raw material of benzoate anion is usually sodium benzoate, which is stable in air, easily soluble in water, low in cost and high in yield. It is also widely used as a food preservative, featuring its safety and abundance. Besides, direct grown binder-free materials circumvent employment of insulating binders, which further boost electrical conductivity. Herein, we report a scalable strategy to in-situ synthesized ultrafine and well-dispersive carbon wrapped NiS nanoparticles anchored on carbon cloth (NiS@C NPs/CC), where the preponderance is that the configuration of well-dispersive nanoparticles with a small diameter vastly shortens ion transport pathway and enlarges expansion space, and the characteristics of carbon confinement and self-assembly synergistically accelerate electric conductivity. The as-obtained NiS@C NPs/CC delivers a superior reversible capacity of 437 mAh g^{-1} at 100 mA g^{-1} and displays long lifespan with a high capacity of 162 mAh g^{-1} after 500 cycles (337 mAh g^{-1} after 50 cycles) at 400 mA g^{-1}.

2. Materials and methods

2.1. Materials synthesis

2.1.1. Synthesis of the electrolyte

All-phenyl complex (APC)-based hybrid electrolyte was prepared according to reported method [43].

2.1.2. In situ generation of benzoate-$Ni(OH)_2$ on CC

0.2 M $Ni(NO_3)_2$ solution (24 mL) and 0.267 M C_6H_5COONa solution (36 mL) were adequately mixed at room temperature. Subsequently, the green solution and a piece of CC (2 cm × 4 cm) were transferred to a 50 mL Teflon-lined stainless steel autoclave. The autoclave was sealed and maintained at 95 °C for 2 h. After the autoclave cooled down at room temperature, the resulting Benzoate-$Ni(OH)_2$/CC was taken out and washed with distilled water and ethanol, followed by drying at 80 °C under vacuum to obtain Benzoate-$Ni(OH)_2$/CC with a loading of ~1.8 mg cm^{-2}.

2.1.3. Synthesis of NiS@C NPs/CC

The NiS@C NPs/CC was synthesized by utilizing benzoate anion as carbon source and Benzoate-$Ni(OH)_2$-templated sulfuration. Typically, the resulting Benzoate-$Ni(OH)_2$/CC precursor and appropriate sulfur powder were put into two separate porcelain boats. After flushed with Ar, the temperature was elevated to 500 °C at a rate of 2 °C min^{-1} and then maintained for 2 h, and then naturally cooled to ambient temperature. The mass loading for NiS@C NPs/CC was about 1.0 mg cm^{-2}.

2.1.4. Synthesis of NiS NSs/CC

NiS NSs/CC was fabricated via employing pure $Ni(OH)_2$ as precursor. In a typical synthesis, $Ni(NO_3)_2{\cdot}6H_2O$ (1.45 g) and Hexamethylenetetramine (HMT; 1.4 g) were dissolved in 36 mL of water under vigorous stirring. Then, the homogenous solution was transferred to a 50 mL Teflon-lined stainless-steel autoclave in which a piece of treated CC was immersed into the solution. The autoclave was sealed and maintained at 100 °C for 10 h to obtain the $Ni(OH)_2$/CC product with a loading of 1.6 mg cm^{-2}. Finally, $Ni(OH)_2$/CC precursor with appropriate sulfur powder were heated to 400 °C for 2 h, and then naturally cooled to room temperature.

2.1.5. Synthesis of NiS@C powder and NiS NSs powder

For TGA analysis, we also prepared corresponding powder samples. Specifically, the synthetic method of powder materials is analogous with binder-free cathodes but without CC substrate. Attentively, the preparation of NiS@C powder is in accord with NiS@C NPs/CC apart from varying the hydrothermal time to 4 h.

2.2. Materials characterizations

The phase structures were studied by XRD (D8 Advance, Bruker AXS) with Cu Kα radiation and Jobin Yvon Horiba Raman spectrometer model HR800, with a 10 mW helium/neon laser at 632.8 nm excitation in the range of 100–2000 cm^{-1}. FTIR (Magna-IR 550 II, Nicolet) analysis was used to verify the functional groups in Benzoate-$Ni(OH)_2$ and the composite. X-ray photoelectron spectroscopy (XPS) was conducted on a Thermo Scientific™ K-Alpha^{TM+} spectrometer equipped with a monochromatic Al Kα X-ray source (1486.6 eV) operating at 100 W. Samples were analyzed under vacuum ($P < 10^{-8}$ mbar) with a pass energy of 150 eV (survey scans) or 25 eV (high-resolution scans). All peaks would be calibrated with C1s peak binding energy at 284.0 eV for adventitious carbon. The morphology of the samples was analyzed using a field emission scanning electron microscope (FE-SEM; JEOL7500FA, Tokyo, Japan). Elemental analysis was performed with an Elementar Vario EL3

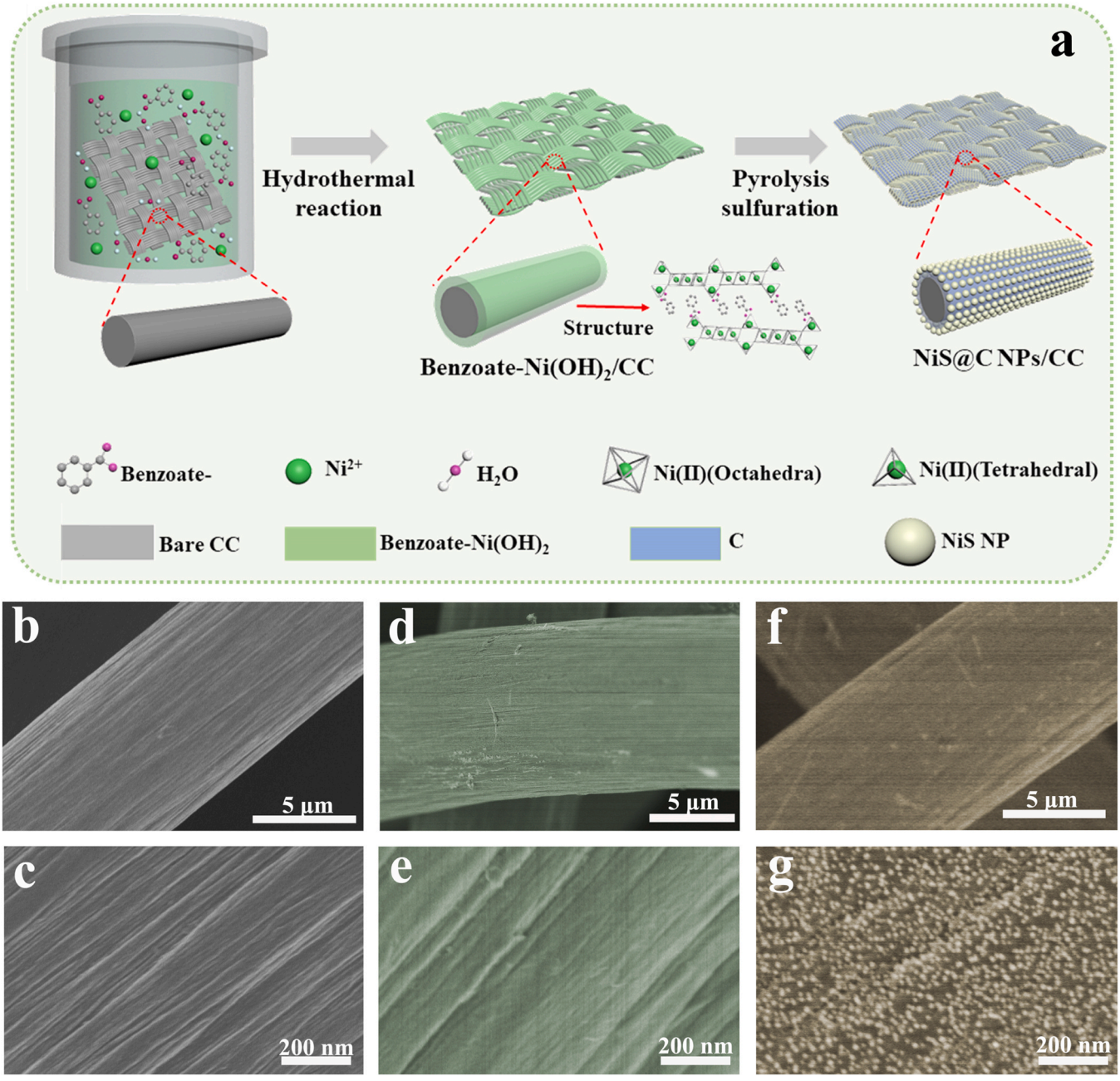

Fig. 1. (a) Schematic illustration of the fabrication for NiS@C NPs/CC. The SEM images of (b,c) bare CC, (d,e) Benzoate-Ni(OH)$_2$/CC and (f,g) NiS@C NPs/CC.

elemental analyzer. Energy-filtered TEM (JEOL 2011 F, Tokyo, Japan) was used to investigate the microstructure and for elemental mapping. Thermogravimetic analysis (TGA, Netzsch STA 449 F3) connected to a mass spectrometer (MS, Hiden HPR 20) was carried out at a ramp rate of 10 °C min^{-1} in air.

2.3. Electrochemical measurements

The electrochemical performances were tested with the use of 2032 coin-type cells in an argon-filled glove box. As-obtained materials were punched into a 12 mm disk as working electrodes. Additionally, the powder electrode was fabricated by coating slurries containing NiS@C active material (80% wt%), Super-P acetylene carbon (10% wt%) and polyvinylidene fluoride (PVDF; 10% wt%) on stainless steel foil. The areal mass loading of active material is about 1 mg cm^{-2}. Magnesium metal and glass fiber were used as counter electrode and separator, respectively. APC-LiCl with high coulombic efficiency, which is widely used in magnesium-based hybrid batteries, was employed as electrolyte. The electrolyte amount for assembling a battery is about 120 μL. Galvanostatic charge/discharge measurements were performed on a multichannel battery testing system within a potential range of 0.1–1.95 V vs. Mg/Mg^{2+}. Cyclic voltammetry (CV) was tested by a CHI 660D electrochemical workstation between 0.1 and 1.95 V vs. Mg/Mg^{2+}. Electrochemical impedance spectroscopy (EIS) was also conducted using a CHI 660D electrochemical workstation. The amplitude was 10 mV, and the applied frequency range was from 100 kHz to 0.01 Hz. All of the tests were carried out at ambient temperature.

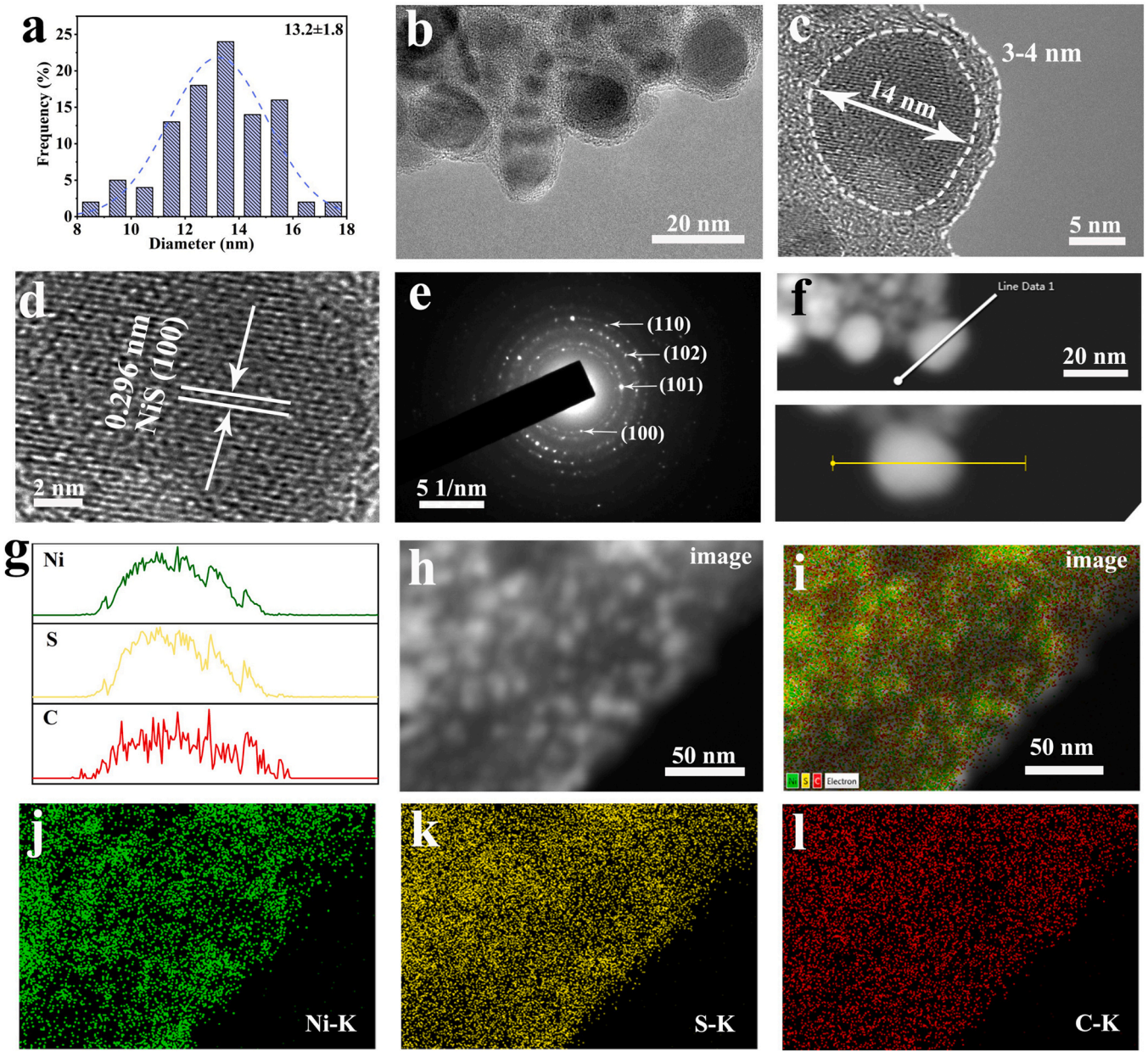

Fig. 2. (a) Corresponding histogram of the NiS size distributions. (b) TEM image of NiS@C NPs scraped down from NiS@C NPs/CC. (c) TEM image of a single NiS particle wrapped by carbon. (d) HRTEM image and (e) SAED pattern of NiS@C NPs. (f) EDS line scan of NiS@C NPs on a STEM image and (g) the corresponding element distributions of Ni, S, and C, respectively. (h) STEM image of NiS@C NPs. (i) STEM image and the corresponding elemental mapping of (j) Ni, (k) S and (l) C.

3. Results and discussion

Fig. 1a elucidates a facile synthetic process of NiS@C NPs/CC schematically. Benzoate anion-intercalated $Ni(OH)_2$ on CC (Benzoate-$Ni(OH)_2$/CC) was uniformly encapsulated on CC substrate by a scalable hydrorhermal reaction. It is worth mentioning that the flexible and inactive features of CC substrate are preferred for practical uses in technological devices. Monodisperse NiS nanoparticles with a well-wrapped carbon (NiS@C NPs) was fabricated via one-step carbonization and sulfuration of Benzoate-$Ni(OH)_2$/CC precursor, where intercalated benzoate anion directly carbonized as a maskant to facilitate electric conductivity and suppress agglomeration. Fig. 1b and c show the scanning electron microscopy (SEM) images of pristine CC, demonstrating a fiber-like morphology and a smooth surface. After a facile hydrorhermal reaction, the as-prepared precursor displays an unchanged morphology (Fig. 1d and e). Intriguingly, the fibrous shape of the CC is well maintained after undergoing pyrolysis and sulfuration process, while the overall surface is uniformly dispersed with ultrafine NiS nanoparticles (Figs. 1f, g and S1). Such feature enables more available superficial area, more complete contact between cathode and electrolyte, larger room for expansion space, and shorer transport distance of ions/electrons, which are all favorable to a better electrochemical performance. For the sake of revealing the advantages of the binder-free electrode, the corresponding powder sample was synthesized by prolongating the hydrothermal time. The SEM images are shown in Fig. S2, suggesting the carbon fiber structure embedded with NiS particles.

Fig. 2a displays the histogram of the NiS size distributions, manifesting an average diameter of 13.2 nm. Fig. 2b depicts the transmission electron microscopy (TEM) image of as-synthesized NiS@C NPs scraped down from NiS@C NPs/CC, suggesting that the monodisperse NiS particles on the CC surface are crosslinked by carbon rather than being separated. The corresponding high-

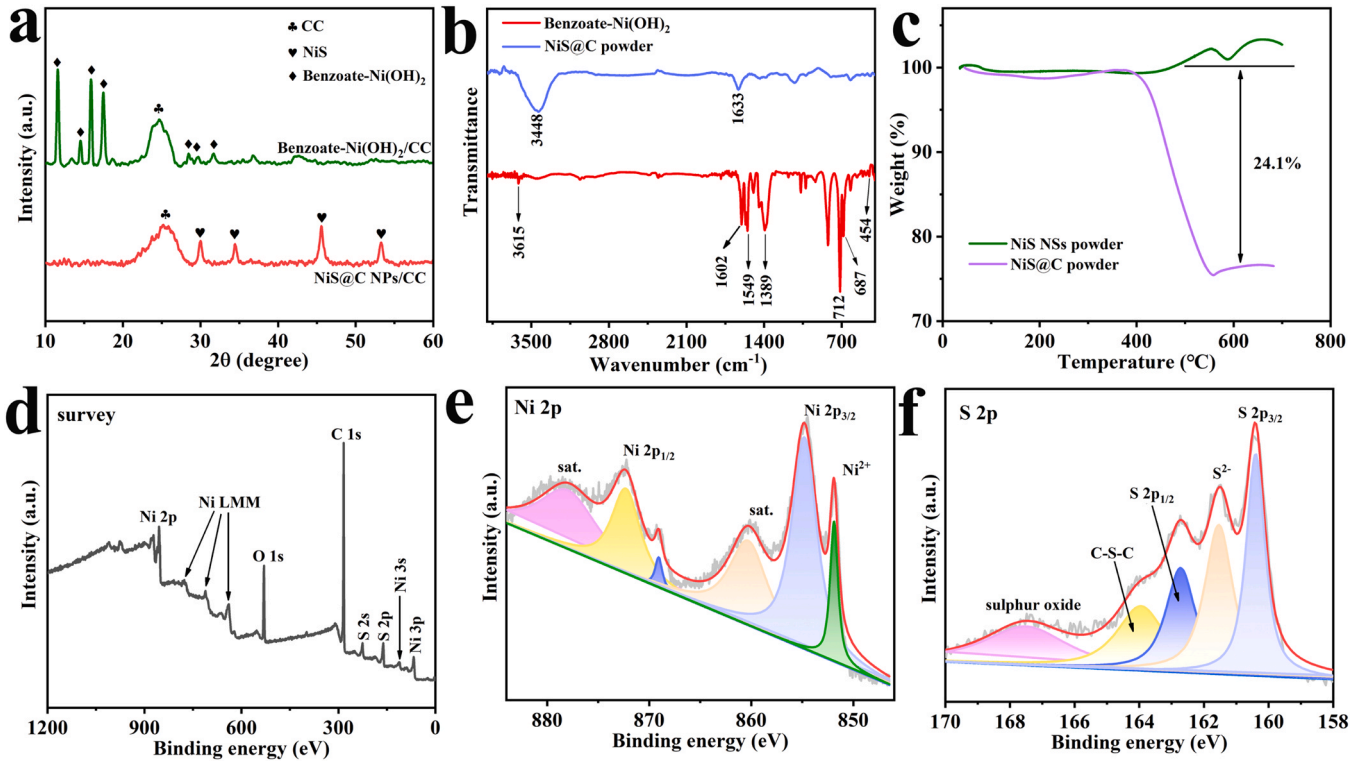

Fig. 3. (a) XRD patterns for Benzoate-Ni(OH)$_2$/CC and NiS@C NPs/CC. (b) FTIR spectra for Benzoate-Ni(OH)$_2$ and NiS@C powder. (c) TGA curves for NiS NSs powder and NiS@C powder. (d) XPS survey spectrum for NiS@C NPs/CC. XPS spectra for NiS@C NPs/CC in the (e) Ni 2p and (f) S 2p regions.

resolution TEM (HRTEM) image shown in Fig. 2c explicitly illustrates that the size of carbon layer in NiS surface is approximately 3–4 nm, and such carbon confinement enhances the electrical conductivity, inhibits aggregation between particles and alleviates the volume expansion. Moreover, the HRTEM image also affirms the characteristics of crystallization and shows lattice fringe of 0.296 nm, indexing to the (100) plane of NiS phase (Fig. 2d). The structure of NiS was also confirmed by selected area electron diffraction (SAED), as shown in Fig. 2e. Specifically, the confirmation of carbon coating in a single NiS@C particle can be further verified by the elemental line-scan profile (Fig. 2f and g), which explains why the diameter of C element in the scan area is larger than that for Ni and S elements. Besides, Fig. 2h-l depict the scanning transmission electron microscopy (STEM) image and the elemental mapping images of Ni, S and C, furnishing more evidence for the homogeneous distribution of NiS@C. For comparison, the SEM images of benzoate anion-free Ni(OH)$_2$/CC are presented in Fig. S3a and b, which reveals that CC is densely packed with thin and smooth Ni(OH)$_2$ nanosheets. Notably, the nanoarchitecture is well preserved after undergoing a sulfuration process. Nanosheets also integrate on the CC substrate perfectly. (Fig. S3c and d).

Fig. 3a shows the X-ray diffraction (XRD) patterns of Benzoate-Ni(OH)$_2$/CC and NiS@C NPs on CC (NiS@C NPs/CC), where a broad and strong diffraction peak at 25.4° can be assigned to CC substrate. The precursor presents characteristic peaks at 11.3°, 14.6°, 15.8°, 17.0°, 28.4°, 29.5° and 31.4°, corresponding to crystalline Ni$(C_6H_5COO)_{1.17}(OH)_{0.83}$ 0.59 H_2O phase (JCPDS no. 42-1835), and the schematic drawing for Benzoate-Ni(OH)$_2$ is shown in Fig. 3b. Combined with the SEM result, it was uncovered that a flat Benzoate-Ni(OH)$_2$ film was evenly coated on CC. After experiencing carbonization and sulfuration process, the as-prepared sulfide product is well in accordance with pure NiS phase with the space group of *P*63/*mmc* (JCPDS no. 02-1280). To probe the role of the benzoate anion, pure Ni(OH)$_2$ was also utilized as a precursor for sulfurization treatment to fabricate pure NiS phase (Fig. S4). Fourier transform infrared (FTIR) measurement was also performed to further confirm the structure of Benzoate-Ni(OH)$_2$/CC and NiS@C NPs/CC. As illustrated in Fig. 3b, the FTIR spectrum of Benzoate-Ni(OH)$_2$ displays a band at 3615 cm^{-1}, indexing to the O-H stretching vibration of free OH groups from a brucite-like structure. The existence of mono-substituted aromatic ring can be well verified by the in-plane skeletal vibration at 1602 cm^{-1} and the two adsorption bands at 712 and 687 cm^{-1} [44]. Two sharp and intense bands located at 1549 and 1389 cm^{-1} are attributed to the asymmetric and symmetric vibrations of the C-O bonds from intercalated benzoate anions. It is noteworthy that there is no corresponding bonds of benzoate anion in the FT-IR spectrum of sulfide product, implying a fully reactive carbonization and sulfuration process. The thermogravimetric analysis (TGA) uncovers that the content of carbon in the Benzoate-Ni(OH)$_2$-derived NiS was determined to be 24.1%, while pure Ni(OH)$_2$-derived NiS was a carbon-free material, indicating a successful conversion from benzoate anion to carbon (Fig. 3c).

The chemical composition and valence states on the surface of NiS@C NPs/CC were investigated by X-ray photoelectron spectroscopy (XPS). The XPS survey spectrum (Fig. 3d) manifests the existence of Ni, S, C and O elements in NiS@C NPs/CC. In the case of high-resolution Ni 2p spectrum (Fig. 3e), the binding energies (BEs) located at 851.9 and 869.1 eV can be assigned to Ni 2p$_{3/2}$ and Ni 2p$_{1/2}$ in NiS [45]. Other peaks at 854.8 and 872.3 eV with two satellite peaks (sat.) can be identified to Ni 2p$_{3/2}$ and Ni 2p$_{1/2}$ in nickel oxide/hydroxide, which is due to the inescapably surface oxidation of as-obtained material [46]. The fitted spectrum of S 2p in Fig. 3f has two peaks with the BEs at 160.4 and 162.7 eV, corresponding to S 2p$_{3/2}$ and S 2p$_{1/2}$, respectively. The BEs located at 161.5 and 163.9 eV can be ascribed to S^{2-} and C-S-C bond in the composite, while an extra peak at 167.5 eV is indexed to the formation of sulfur oxide [45,47,48]. The BE at 283.6 eV can be attributed to non-oxygenated C (C-C). All results above affirm the as-fabricated material is NiS@C.

First, a simple test of the electrochemical performance of NiS@C NPs/CC in pure MIBs was performed. As can be seen from the Fig. S6,

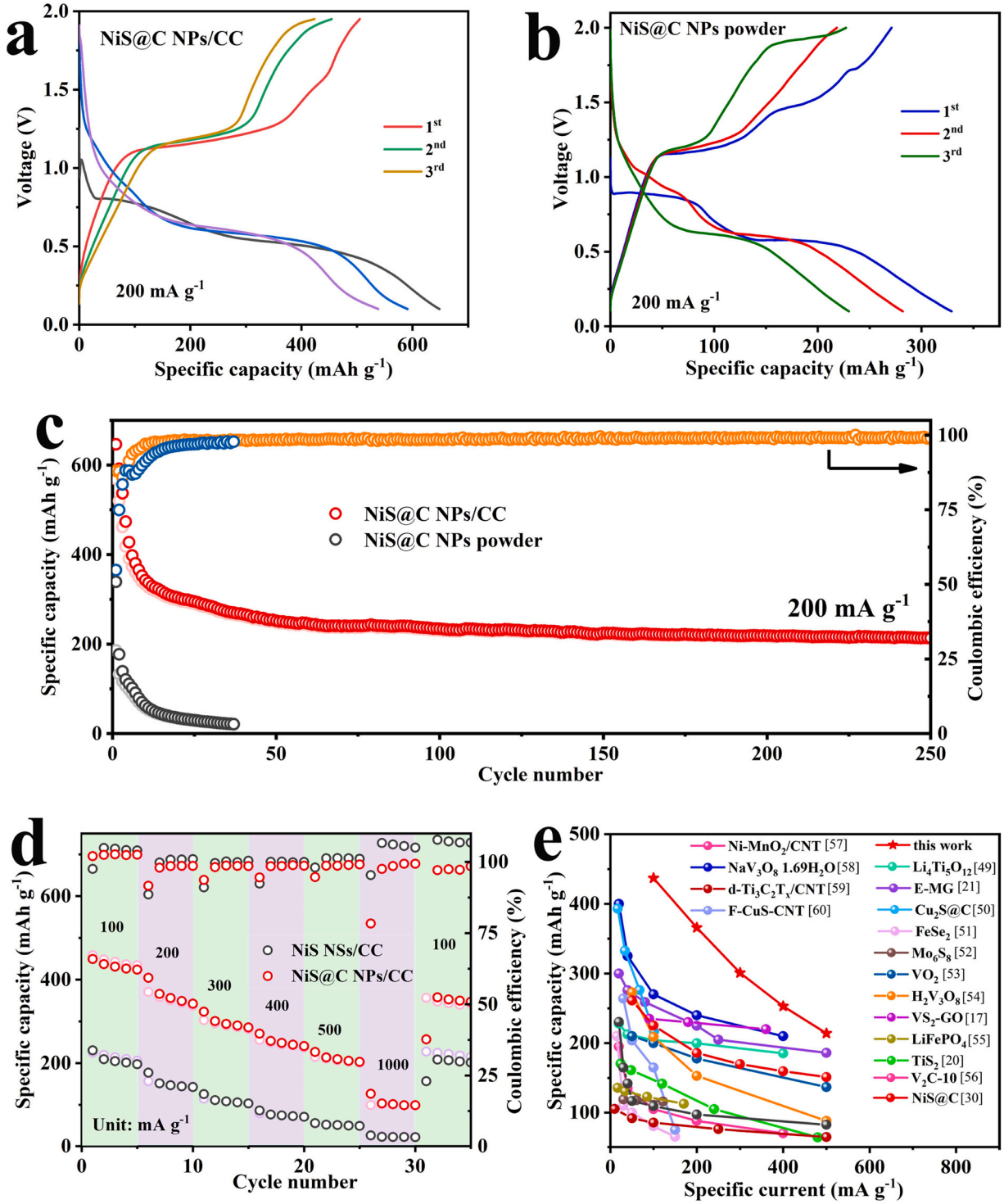

Fig. 4. Galvanostatic charge-discharge voltage profiles of (a) NiS@C NPs/CC and (b) NiS@C NPs powder. (c) Cycling performance and coulombic efficiency at a current density of 200 mA g^{-1}. (d) Rate performance and coulombic efficiency of NiS@C NPs powder and NiS@C NPs/CC. (e) Comparison of reversible capacity of the state-of-the-art cathodes for reported Mg^{2+}/Li^{+} hybrid battery systems.

NiS@C NPs/CC exhibits poor performance in pure Mg^{2+} electrolyte. Subsequently, the performance of as-prepared cathode materials are investigated in MLIBs. Figs. 4 and S7 underlines the electrochemical performance of NiS NSs/CC and NiS@C NPs/CC cathodes in MLIBs. The typical charge/discharge profiles for NiS NSs/CC and NiS@C NPs/CC with a voltage of 0.1–1.95 V and a current density of 200 mA g^{-1} are shown in Figs. 4a and S7a, respectively. The discharge plateau voltages for NiS NSs/CC are 0.78 V and 0.6 V and the initial discharge capacity is 342 mAh g^{-1}. After three cycles, the plateau corresponding to 0.78 V disappeared, and the discharge specific capacity was declined to 203 mAh g^{-1}, suggesting a small plateau capacity and low reversible discharge capacity. Homoplastically, the NiS@C NPs/CC has two obvious plateaus at 0.8 V and 0.6 V in the first cycle at the same current density, and delivers an initial discharge capacity of 647 mAh g^{-1}. Attentively, in subsequent cycle, the only discharge plateau is still located at about 0.6 V, implementing an eminent discharge capacity of 538 mAh g^{-1} in third cycle. In addition, the charge-discharge voltage profile of NiS@C NPs/CC after

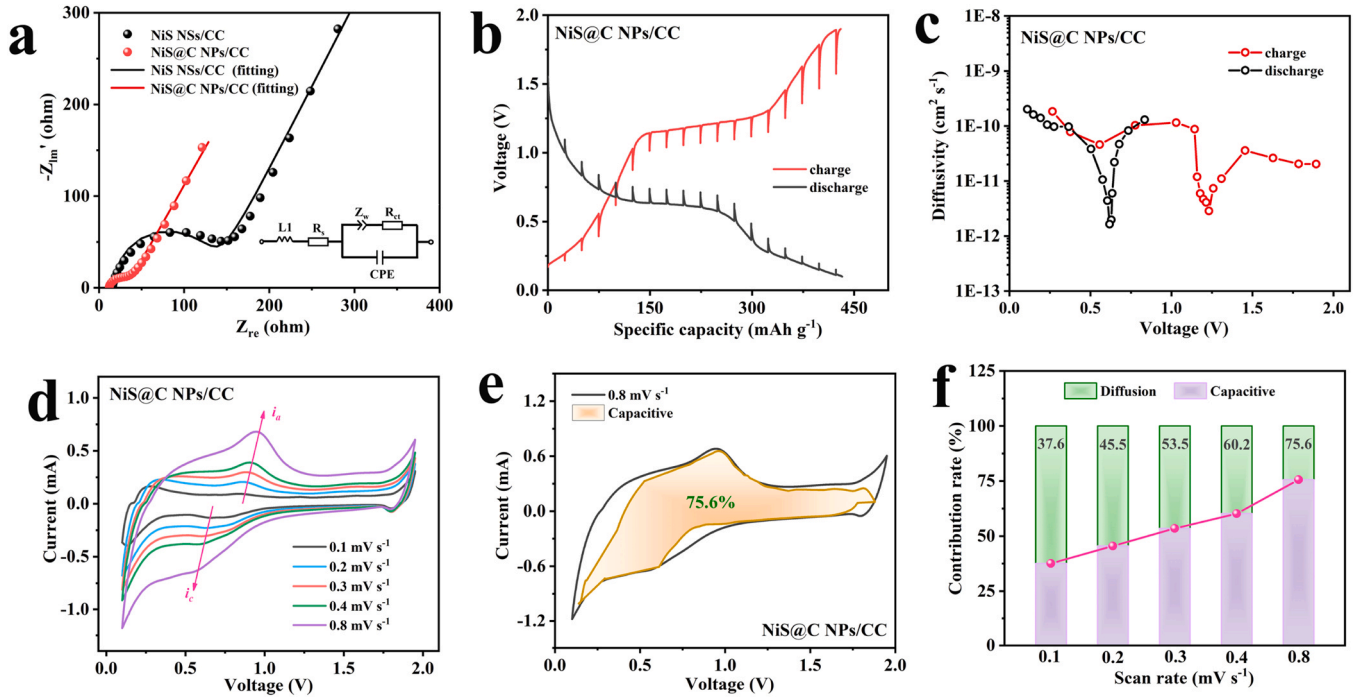

Fig. 5. (a) EIS plots of NiS NSs/CC and NiS@C NPs/CC. (b) GITT profile of NiS@C NPs/CC at 50 mA g^{-1}. (c) Corresponding calculated Mg^{2+}/Li^{+} diffusion coefficients. (d) CV curves at various scan rates from 0.1 to 0.8 mV s^{-1}. (e) Separation of capacitive and diffusion contribution at 0.8 mV s^{-1}. (f) Percentages of capacitive contribution at different scan rates.

200th cycles is also demonstrated in Fig. S8. Importantly, compared with NiS NSs/CC, NiS@C NPs/CC exhibits a much higher initial coulombic efficiency (CE; 64% and 88% for NiS NSs/CC and NiS@C NPs/CC, respectively). The markedly increased specific capacities of NiS@C NPs/CC can be ascribed to the uniquely ultrafine and homogeneous nanoparticle feature and the in situ coated carbon. In terms of NiS@C NPs powder electrode, the charge-discharge curves display the same shape as the corresponding binder-free electrode, but exhibits faster capacity decay (Fig. 4b). As the cyclic stability is the overriding consideration for conversion materials, Figs. 4c and S7b underlines the comparison between NiS@C NPs powder, NiS@C NPs/CC and NiS NSs/CC at 200 mA g^{-1}. The CEs of NiS NSs/CC and NiS@C NPs/CC are stabilized at above 99% other than the first 10 cycles. The NiS NSs/CC shows low discharge capacities and attains 110 mAh g^{-1} after undergoing 100 cycles, whereas the NiS@C NPs/CC reveals superior capacity retention over that for NiS NSs/CC, with much higher specific capacities of 235 and 214 mAh g^{-1} after 100 and 250 cycles. Obviously, NiS@C NPs powder has a much shorter lifespan, which can be mainly ascribed to the introduction of binders during the fabrication of such powder electrodes. A biggish difference of capacities between NiS NSs/CC and NiS@C NPs/CC is undoubtedly morphologic discrepancy and the addition of carbon, but both of which exhibit excellent durability. By comparing the cycling curve of corresponding powder cathode, we owes this to the utilization of binder-free cathodes.

Even more significantly, rate capability is a more vital method to evaluate the practical availability of cathode materials. In consequence, the rate performance of as-fabricated two cathodes was tested at various current densities (Fig. 4d), realizing discharge capacities of 209, 152, 100, 77, 52 and 23 mAh g^{-1} at 100, 200, 300, 400, 500 and 1000 mA g^{-1}, respectively for the NiS NSs/CC sample. Amazingly, the NiS@C NPs/CC delivers more outstanding performance, which can accomplish discharge capacities of 437, 366, 301, 253, 214 and 103 mAh g^{-1} at the same current densities. Fig. 4e extrudes the exceptional reversible capacity and the admirable rate capability of this work in comparison with other reported hybrid batteries [17,20,21,30,49–60]. Moreover, two kind of binder-free cathodes were also investigated at 400 mA g^{-1} and the electrochemical activity of NiS@C NPs/CC can be well maintained even experiencing 600 cycles (Fig. S9), verifying an excellent lifespan. The SEM images of NiS NSs/CC and NiS@C NPs/CC in Fig. S10 display that morphology of NiS@C NPs/CC is also well kept after undergoing 50 cycles, but particle size of which grows up obviously after 500 cycles. In contrast, the architecture of NiS NSs/CC emerges tremendous change, where the original thin nanosheet are aggregated laterally and the thickness is increased to 280 nm after 50 cycles. However, the horizontal space is still maintained in the whole structure. It is worth noting that the morphology of NiS NSs/CC is severely damaged after 500 cycles, indicating that one-dimensional nanoparticles have more lateral expansion space than two-dimensional nanosheets and the carbon encapsulation can better restrain the aggregation.

Fig. 5a shows the electrochemical impedance spectra (EIS) analysis, which was conducted to intrinsically investigate the ion diffusion kinetics of NiS NSs/CC and NiS@C NPs/CC. The equivalent circuit in the inset of Fig. 5a is applied to fit the EIS plots, where the R_s is employed to denote the ohm impedance between electrolyte and cell components and R_{ct} signifies the charge-transfer resistance. From the fitting calculation, the values of R_s for NiS@C NPs/CC and NiS NSs/CC are 12.6 and 17.1 Ω, respectively, suggesting small difference in this category of impedance for binder-free cathode. Attentions are worth to paid to the results of R_{ct}, which are calculated as 21.4 and 118.5 Ω for NiS@C NPs/CC and NiS NSs/CC, respectively, clarifying lower charge-transfer resistance and easier ion diffusivity within NiS@C NPs/CC electrode. Moreover, other EIS fitting results are demonstrated in Table S2. These results can be ascribed to the uniform coating of highly conductive carbon and the short ion diffusion distance of one-dimensional particles. In addition, the EIS plot of NiS@C NPs powder sample in MLIBs presented in Fig. S11 verifies faster electron/ion transport in binder-free electrode material, which can be attributed to the avoidance of inactive binders. For the sake of furnishing further insight for excellent conductivity of NiS@C NPs/CC, the Li^{+}/Mg^{2+} solid-state diffusion in NiS@C NPs/CC was probed via galvanostatic intermittent titration technique (GITT) [61–64].

From the voltage profile of a single step in Fig. S12, an equilibrium state has been extremely approached after an open-circuit relaxation for 30 min at 50 mA g^{-1}. Therefore, the GITT curves in Fig. 5b were conducted at an unaltered current pulse of 50 mA g^{-1} for 30 min followed by an open-circuit relaxation for 30 min. The NiS@C NPs/CC cathode implements a discharge specific capacity of 432 mA h g^{-1} in the second cycle. Whereafter, the Mg^{2+}/Li^{+} diffusivity D^{GITT} can be calculated according to recorded GITT curves using the following formula:

$$D^{GITT} = \frac{4}{\pi\tau}\left(\frac{m_B V_M}{M_B S}\right)^2\left(\frac{\Delta E_S}{\Delta E_\tau}\right)^2 \quad (1)$$

where τ, m_B, V_M, M_B, and S are on behalf of the pulse time, mass loading, molar volume, molar mass and electrode–electrolyte interface area, respectively. ΔEs and ΔEt are the voltage change induced by the pulse current and galvanostatic discharging-charging. Fig. 5c demonstrates the calculated diffusion coefficients at different voltages during discharge and charge process, and the calculated values of NiS@C NPs/CC go from 10^{-10} to 10^{-12} and back to 10^{-10} cm^2 s^{-1} during the discharge stage and an analogous pattern is occurred at charge process, indicating an average diffusion coefficient of 5.8×10^{-11} cm^2 s^{-1}.

Electrochemical reaction kinetics of NiS@C NPs/CC was also researched via CV measurement under diverse scan rates ranging from 0.1 to 0.8 mV s^{-1} within 0.1–1.95 V. All the CV curves depicted in Fig. 5d have a similar shape, but present a significantly enhanced oxidation peaks and greater polarization. Specifically, before testing the CV curves in Fig. 5d, multiple cycle tests were performed. As a result, the redox peaks in Fig. 5d can be well corresponded to the voltage plateau in Fig. S8. The charge-storage mechanism can be estimated by $i = av^b$ [65], in which b value fitted by the slope of $\log(v)$ vs $\log(i)$ is calculated between 0.5 and 1.0. Reaction is diffusion-controlled if the value is close to 0.5, while considered to be a capacitive behavior if close to 1.0. Fig. S13 displays that the b values for reduction and oxidation peaks are 0.73 and 0.77, respectively, elucidating the combination of the diffusive and capacitive controlled the reaction. Additionally, the quantified capacitive and diffusion contribution can be determined at a fixed scan rate via the equation $i = k_1v + k_2v^{1/2}$ (where k_1v signifies the capacitive current and $k_2v^{1/2}$ is on behalf of the diffusion-controlled current). The calculation result indicates that the capacitive contribution at 0.1, 0.2, 0.3, 0.4 and 0.8 mV s^{-1} enhances from 37.6% to 75.6% (Fig. 5f). The pseudocapacitive contribution of NiS@C NPs/CC in Fig. 5e accounts for 75.6% at 0.8 mV s^{-1} and such high capacitive contribution avails to the charge transfer kinetics and to good rate performance. Moreover, the electrode kinetics of NiS@C NPs/CC after 10, 20 and 50 cycles are shown in Fig. S14, uncovering a decreased semicircle diameter and an increased line slope with the cycles increasing. This analysis elucidates that the interface between electrolyte and cathode greatly reduces the impedance and such interface has an impressive stability, which accounts for the good cycling performance of NiS@C NPs/CC clearly.

4. Conclusions

In summary, ultrafine and well-dispersive carbon encapsulated NiS nanoparticles were successfully fabricated via one-step carbonization and sulfuration of organic anion-intercalated precursor. Such material synergistically shortens diffusion distances, alleviates volume expansion and prevents material pulverization by maximizing the merits of fine nanoparticles, carbon conductive networks and binder-free electrodes. Consequently, the as-obtained binder-free conversion cathode material exhibits excellent Mg^{2+}/Li^{+} storage behavior, gaining a high reversible capacity of 437 mAh g^{-1} at 100 mA g^{-1} and excellent cycle stability. This finding not only affirms the feasibility of a novel binder-free cathode material in MLIBs except for copper based chalcogenide, but would also open up a new avenue for the rational design of well-dispersive nanomaterials derived from intercalated organic-anion for applications.

CRediT authorship contribution statement

Guilei Zhu: Methodology, Writing – original draft, Writing – review & editing, Validation, Formal analysis, Investigation. **Wenbin Wang:** Writing – Review & Editing, Validation. **Xuebin Yu:** Supervision, Writing – review & editing, Resources, Funding acquisition, Project administration.

Declaration of Competing Interest

The authors declare that they have no known competing financial interests or personal relationships that could have appeared to influence the work reported in this paper.

Acknowledgments

This work was partially supported by the National Key Research and Development Program of China (2017YFA0204600), the National Science Fund for Distinguished Young Scholars (51625102), the National Natural Science Foundation of China (51971065), and the Innovation Program of Shanghai Municipal Education Commission (2019-01-07-00-07-E00028).

Appendix A. Supplementary material

Supplementary data associated with this article can be found in the online version at doi:10.1016/j.jallcom.2022.165835.

References

[1] J. Muldoon, C.B. Bucur, T. Gregory, Quest for nonaqueous multivalent secondary batteries: magnesium and beyond, Chem. Rev. 114 (2014) 11683–11720.
[2] P. Canepa, G. Sai Gautam, D.C. Hannah, R. Malik, M. Liu, K.G. Gallagher, K.A. Persson, G. Ceder, Odyssey of multivalent cathode materials: open questions and future challenges, Chem. Rev. 117 (2017) 4287–4341.
[3] H.D. Yoo, I. Shterenberg, Y. Gofer, G. Gershinsky, N. Pour, D. Aurbach, Mg rechargeable batteries: an on-going challenge, Energy Environ. Sci. 6 (2013) 2265.
[4] M. Armand, J.M. Tarascon, Building better batteries, Nature 451 (2008) 652–657.
[5] M. Mao, T. Gao, S. Hou, C. Wang, A critical review of cathodes for rechargeable Mg batteries, Chem. Soc. Rev. 47 (2018) 8804–8841.
[6] G. Li, B. Huang, Z. Pan, X. Su, Z. Shao, L. An, Advances in three-dimensional graphene-based materials: configurations, preparation and application in secondary metal (Li, Na, K, Mg, Al)-ion batteries, Energy Environ. Sci. 12 (2019) 2030–2053.
[7] J. Muldoon, C.B. Bucur, T. Gregory, Fervent hype behind magnesium batteries: an open call to synthetic chemists-electrolytes and cathodes needed, Angew. Chem. Int. Ed. 56 (2017) 12064–12084.
[8] Y. Shen, Q. Zhang, Y. Wang, L. Gu, X. Zhao, X. Shen, A pyrite iron disulfide cathode with a copper current collector for high-energy reversible magnesium-ion storage, Adv. Mater. 33 (2021) 2103881.
[9] A. Du, Z. Zhang, H. Qu, Z. Cui, L. Qiao, L. Wang, J. Chai, T. Lu, S. Dong, T. Dong, H. Xu, X. Zhou, G. Cui, An efficient organic magnesium borate-based electrolyte with non-nucleophilic characteristics for magnesium-sulfur battery, Energy Environ. Sci. 10 (2017) 2616–2625.
[10] Y.L. Shen, Y.J. Wang, Y.C. Miao, M. Yang, X.Y. Zhao, X.D. Shen, High-energy interlayer-expanded copper sulfide cathode material in non-corrosive electrolyte for rechargeable magnesium batteries, Adv. Mater. 32 (2020) 1905524.
[11] D. Chen, F. Du, S.-a. Cao, T. Li, F. Xu, $Co_{0.85}Se$ hollow polyhedrons entangled by carbon nanotubes as a high-performance cathode for magnesium secondary batteries, Chem. Eng. J. 428 (2022) 129545.
[12] F. Liu, T. Wang, X. Liu, N. Jiang, L.-Z. Fan, High-performance heterojunction Ti_3C_2/$CoSe_2$ with both intercalation and conversion storage mechanisms for magnesium batteries, Chem. Eng. J. 426 (2021) 130747.
[13] Y. Zhang, L. Huang, X. Zhou, Y. Luo, Q. Chen, Y. Chen, The performance and mechanism of copper-cobalt sulfide cathode for hybrid Mg^{2+}/Li^{+} batteries, J. Alloy. Compd. 881 (2021).
[14] M. Vincent, V.S. Avvaru, M. Haranczyk, V. Etacheri, High-performance Mg-Li hybrid batteries based on pseudocapacitive anatase $Ti_{1-x}Co_xO_{2-y}$ nanosheet cathodes, ChemSusChem (2022) e202102562.

[15] M. Rashad, H. Zhang, X. Li, H. Zhang, Fast kinetics of Mg^{2+}/Li^{+} hybrid ions in a polyanion $Li_3V_2(PO_4)_3$ cathode in a wide temperature range, J. Mater. Chem. A 7 (2019) 9968–9976.

[16] H. Xu, X. Zhang, T. Xie, Z. Li, F. Sun, N. Zhang, H. Chen, Y. Zhu, X. Zou, C. Lu, J. Zou, R.M. Laine, Li^{+} assisted fast and stable Mg^{2+} reversible storage in cobalt sulfide cathodes for high performance magnesium/lithium hybrid-ion batteries, Energy Storage Mater. 46 (2022) 583–593.

[17] X. Hu, J. Peng, F. Xu, M. Ding, Rechargeable Mg^{2+}/Li^{+}, Mg^{2+}/Na^{+}, and Mg^{2+}/K^{+} hybrid batteries based on layered VS_2, ACS Appl. Mater. Interfaces 13 (2021) 57252–57263.

[18] X. Hu, J. Peng, F. Xu, M. Ding, Rechargeable Mg^{2+}/Li^{+}, Mg^{2+}/Na^{+}, and Mg^{2+}/K^{+} Hybrid batteries based on layered VS_2, ACS Appl. Mater. Interfaces 13 (2021) 57252–57263.

[19] Y. Gu, Y. Katsura, T. Yoshino, H. Takagi, K. Taniguchi, Rechargeable magnesium-ion battery based on a $TiSe_2$-cathode with d-p orbital hybridized electronic structure, Sci. Rep. 5 (2015) 12486.

[20] T. Gao, F. Han, Y. Zhu, L. Suo, C. Luo, K. Xu, C. Wang, Hybrid Mg^{2+}/Li^{+} battery with long cycle life and high rate capability, Adv. Energy Mater. 5 (2015) 1401507.

[21] X. Yu, G. Zhao, C. Liu, H. Huang, X. Shen, N. Zhang, A material of hierarchical interlayer-expanded MoS_2 nanosheets/hollow N-doped carbon nanofibers as a promising Li^{+}/Mg^{2+} co-intercalation host, J. Mater. Chem. A 9 (2021) 11545–11552.

[22] X. Yu, G. Zhao, H. Huang, C. Liu, P. Lyu, N. Zhang, Interlayer-expanded MoS_2 nanoflowers anchored on the graphene: a high-performance Li^{+}/Mg^{2+} co-intercalation cathode material, Chem. Eng. J. 428 (2022) 131214.

[23] Y. Ma, K. Shuai, L. Zhou, J. Wang, Q. Wang, Effect of Mg^{2+} and Mg^{2+}/Li^{+} electrolytes on rechargeable magnesium batteries based on an erythrocyte-like CuS cathode, Dalton Trans. 49 (2020) 15397–15403.

[24] T. Li, A. Qin, H. Wang, M. Wu, Y. Zhang, Y. Zhang, D. Zhang, F. Xu, A high-performance hybrid Mg^{2+}/Li^{+} battery based on hierarchical copper sulfide microflowers conversion cathode, Electrochim. Acta 263 (2018) 168–175.

[25] H. Yuan, N. Wang, Y. NuLi, J. Yang, J. Wang, Hybrid Mg^{2+}/Li^{+} batteries with Cu_2Se cathode based on displacement reaction, Electrochim. Acta 261 (2018) 503–512.

[26] W. Wang, Y. Yang, Y. NuLi, J. Zhou, J. Yang, J. Wang, Metal organic framework (MOF)-derived carbon-encapsulated cuprous sulfide cathode based on displacement reaction for hybrid Mg^{2+}/Li^{+} batteries, J. Power Sources 445 (2020).

[27] Y. Zhang, J. Xie, Y. Han, C. Li, Dual-salt Mg-based batteries with conversion cathodes, Adv. Funct. Mater. 25 (2015) 7300–7308.

[28] X. Cai, L. Yu, J. Dong, Y. Cen, T. Zhu, D. Yu, C. Chen, D. Zhang, Y. Liu, F. Pan, Revealing the electrochemical mechanism of the conversion-type Co_3S_4 in a novel high-capacity Mg-Li hybrid battery, Electrochim. Acta 401 (2022) 139403.

[29] C. Liu, G. Zhao, L. Zhang, X. Yu, H. Huang, K. Sun, N. Zhang, A hybrid Mg^{2+}/Li^{+} battery based on high-capacity conversion-type cobalt disulfide cathodes with ultralong cycle life and high energy density, Chem. Eng. J. 405 (2021) 126726.

[30] G. Zhu, G. Xia, H. Pan, X. Yu, Size-controllable nickel sulfide nanoparticles embedded in carbon nanofibers as high-rate conversion cathodes for hybrid Mg-based battery, Adv. Sci. (2022) e2106107.

[31] C. Ye, L. Zhang, C. Guo, D. Li, A. Vasileff, H. Wang, S.Z. Qiao, A 3D hybrid of chemically coupled nickel sulfide and hollow carbon spheres for high performance lithium-sulfur batteries, Adv. Funct. Mater. 27 (2017) 1702524.

[32] D. Zhang, W.P. Sun, Y. Zhang, Y.H. Dou, Y.Z. Jiang, S.X. Dou, Engineering hierarchical hollow nickel sulfide spheres for high-performance sodium storage, Adv. Funct. Mater. 26 (2016) 7479–7485.

[33] A.A. AbdelHamid, X.F. Yang, J.H. Yang, X.J. Chen, J.Y. Ying, Graphene-wrapped nickel sulfide nanoprisms with improved performance for Li-ion battery anodes and supercapacitors, Nano Energy 26 (2016) 425–437.

[34] Q.D. Li, L. Li, P.J. Wu, N. Xu, L. Wang, M. Li, A. Dai, K. Amine, L.Q. Mai, J. Lu, Silica restricting the sulfur volatilization of nickel sulfide for high-performance lithium-ion batteries, Adv. Energy Mater. 9 (2019) 9.

[35] D. He, Y. Zhang, D. Cao, M. Sun, J. Xia, Y. Yang, Y. Ding, H. Chen, A flexible free-standing FeF_3/reduced graphene oxide film as cathode for advanced lithium-ion battery, J. Alloy. Compd. 909 (2022) 164702.

[36] D. Lan, Y. Zhao, Y. Liu, W. He, N. Zhu, J. Cui, Nano-MnS@ N doped lignite derived carbon composites as superior anode material for sodium-ion batteries, J. Alloy. Compd. 912 (2022) 165083.

[37] M. Xia, G. Rao, H. Wang, J. Ma, J. Wang, X. Jian, Carbon nanocapsules stabilized Cu_2O nanocubes as the high-performance electrode material for metal ion battery, J. Alloy. Compd. 909 (2022) 164714.

[38] Y. Xie, H. Zhang, K. Wu, X. Wang, D. Xiong, M. He, Fe_3C encapsulated in N-doped carbon as potassium ion battery anode with high capacity and long-term cycling performance, J. Alloy. Compd. 910 (2022) 164845.

[39] D. Zhang, W. Su, Z. Li, Q. Wang, F. Yuan, H. Sun, Y. Li, Y. Zhang, B. Wang, Three-dimensional interconnected porous carbon nanoflakes with improved electron transfer and ion storage for lithium-ion batteries, J. Alloy. Compd. 904 (2022).

[40] L.Z. Ouyang, Z.J. Cao, L.L. Li, H. Wang, J.W. Liu, D. Min, Y.W. Chen, F.M. Xiao, R.H. Tang, M. Zhu, Enhanced high-rate discharge properties of $La_{11.3}Mg_{6.0}Sm_{7.4}Ni_{61.0}Co_{7.2}Al_{7.1}$ with added graphene synthesized by plasma milling, Int. J. Hydrog. Energ. 39 (2014) 12765–12772.

[41] C. Lin, L. Yang, L. Ouyang, J. Liu, H. Wang, M. Zhu, A new method for few-layer graphene preparation via plasma-assisted ball milling, J. Alloy. Compd. 728 (2017) 578–584.

[42] M. Ma, R.X. Ge, X.Q. Ji, X. Ren, Z. Liu, A.M. Asiri, X.P. Sun, Benzoate anions-intercalated layered nickel hydroxide nanobelts array: an earth-abundant electrocatalyst with greatly enhanced oxygen evolution activity, ACS Sustain. Chem. Eng. 5 (2017) 9625–9629.

[43] G. Zhu, G. Xia, X. Yu, Hierarchical 3D cuprous sulfide nanoporous cluster arrays self-assembled on copper foam as a binder-free cathode for hybrid magnesium-based batteries, Small (2021) e2101845.

[44] U. Costantino, V. Bugatti, G. Gorrasi, F. Montanari, M. Nocchetti, L. Tammaro, V. Vittoria, New polymeric composites based on poly(-caprolactone) and layered double hydroxides containing antimicrobial species, ACS Appl. Mater. Interfaces 1 (2009) 668–677.

[45] H. Sun, D. Qin, S. Huang, X. Guo, D. Li, Y. Luo, Q. Meng, Dye-sensitized solar cells with NiS counter electrodes electrodeposited by a potential reversal technique, Energy Environ. Sci. 4 (2011) 2630.

[46] D.L. Legrand, H.W. Nesbitt, G.M. Bancroft, X-ray photoelectron spectroscopic study of a pristine millerite (NiS) surface and the effect of air and water oxidation, Am. Miner. 83 (1998) 1256–1265.

[47] X. Gao, J. Wang, D. Zhang, K. Adair, K. Feng, N. Sun, H. Zheng, H. Shao, J. Zhong, Y. Ma, X. Sun, X. Sun, Carbon coated bimetallic sulfide nanodots/carbon nanorod heterostructure enabling long-life lithium-ion batteries, J. Mater. Chem. A 5 (2017) 25625–25631.

[48] R.C. Jin, Y.T. Jiang, G.H. Li, Y.F. Meng, Amorphous carbon coated multiwalled carbon nanotubes@transition metal sulfides composites as high performance anode materials for lithium ion batteries, Electrochim. Acta 257 (2017) 20–30.

[49] M. Rashad, M. Asif, Understanding the low temperature electrochemistry of magnesium-lithium hybrid ion battery in all-phenyl-complex solutions, J. Energy Chem. 56 (2021) 383–390.

[50] W. Wang, Y. Yang, Y. NuLi, J. Zhou, J. Yang, J. Wang, Metal organic framework (MOF)-derived carbon-encapsulated cuprous sulfide cathode based on displacement reaction for hybrid Mg^{2+}/Li^{+} batteries, J. Power Sources 445 (2020) 227325.

[51] C. Zhang, L. Zhang, N. Li, X. Zhang, Studies of $FeSe_2$ cathode materials for Mg-Li hybrid batteries, Energies 13 (2020) 4375.

[52] Y. Cheng, Y. Shao, J.G. Zhang, V.L. Sprenkle, J. Liu, G. Li, High performance batteries based on hybrid magnesium and lithium chemistry, Chem. Commun. 50 (2014) 9644–9646.

[53] C. Pei, F. Xiong, J. Sheng, Y. Yin, S. Tan, D. Wang, C. Han, Q. An, L. Mai, VO_2 nanoflakes as the cathode material of hybrid magnesium-lithium-ion batteries with high energy density, ACS Appl. Mater. Interfaces 9 (2017) 17060–17066.

[54] M. Rastgoo-Deylami, M.S. Chae, S.-T. Hong, $H_2V_3O_8$ as a high energy cathode material for nonaqueous magnesium-ion batteries, Chem. Mater. 30 (2018) 7464–7472.

[55] Y. Cheng, D. Choi, K.S. Han, K.T. Mueller, J.G. Zhang, V.L. Sprenkle, J. Liu, G. Li, Toward the design of high voltage magnesium-lithium hybrid batteries using dual-salt electrolytes, Chem. Commun. 52 (2016) 5379–5382.

[56] F. Liu, Y. Liu, X. Zhao, K. Liu, H. Yin, L.Z. Fan, Prelithiated V_2C MXene: a high-performance electrode for hybrid magnesium/lithium-ion batteries by ion co-intercalation, Small 16 (2020) e1906076.

[57] M. Asif, M. Rashad, Z. Ali, H. Qiu, W. Li, L. Pan, Y. Hou, Ni-doped MnO_2/CNT nanoarchitectures as a cathode material for ultra-long life magnesium/lithium hybrid ion batteries, Mater. Today Energy 10 (2018) 108–117.

[58] M. Rashad, X. Li, H. Zhang, Magnesium/lithium-ion hybrid battery with high reversibility by employing NaV_3O_8 $1.69H_2O$ nanobelts as a positive electrode, ACS Appl. Mater. Interfaces 10 (2018) 21313–21320.

[59] A. Byeon, M.-Q. Zhao, C.E. Ren, J. Halim, S. Kota, P. Urbankowski, B. Anasori, M.W. Barsoum, Y. Gogotsi, Two-dimensional titanium carbide MXene as a cathode material for hybrid magnesium/lithium-ion batteries, ACS Appl. Mater. Interfaces 9 (2016) 4296–4300.

[60] Y. Zhang, Y. Li, Y. Wang, R. Guo, W. Liu, H. Pei, G. Yin, D. Ye, S. Yu, J. Xie, A flexible copper sulfide@multi-walled carbon nanotubes cathode for advanced magnesium-lithium-ion batteries, J. Colloid Interface Sci. 553 (2019) 239–246.

[61] Q. An, Y. Li, H. Deog Yoo, S. Chen, Q. Ru, L. Mai, Y. Yao, Graphene decorated vanadium oxide nanowire aerogel for long-cycle-life magnesium battery cathodes, Nano Energy 18 (2015) 265–272.

[62] Y. Xu, C. Zhang, M. Zhou, Q. Fu, C. Zhao, M. Wu, Y. Lei, Highly nitrogen doped carbon nanofibers with superior rate capability and cyclability for potassium ion batteries, Nat. Commun. 9 (2018) 1720.

[63] W. Weppner, R.A. Huggins, Determination of kinetic-parameters of mixed-conducting electrodes and application to system Li_3Sb, J. Electrochem. Soc. 124 (1977) 1569–1578.

[64] X. Sun, P. Bonnick, V. Duffort, M. Liu, Z. Rong, K.A. Persson, G. Ceder, L.F. Nazar, A high capacity thiospinel cathode for Mg batteries, Energy Environ. Sci. 9 (2016) 2273–2277.

[65] T. Brezesinski, J. Wang, S.H. Tolbert, B. Dunn, Ordered mesoporous alpha-MoO_3 with iso-oriented nanocrystalline walls for thin-film pseudocapacitors, Nat. Mater. 9 (2010) 146–151.